

Additive Manufacturing of Two-Dimensional Conductive Metal–Organic Framework with Multidimensional Hybrid Architectures for High-Performance Energy Storage

Jingxin Zhao,[#] Yan Zhang,[#] Hongyu Lu,[#] Yafei Wang,[#] Xu Dong Liu, Hirbod Maleki Kheimeh Sari, Jianhong Peng,^{*} Shufan Chen, Xifei Li,^{*} Yongjun Zhang, Xueliang Sun,^{*} and Bingang Xu^{*}



Cite This: *Nano Lett.* 2022, 22, 1198–1206



Read Online

ACCESS |



Metrics & More



Article Recommendations

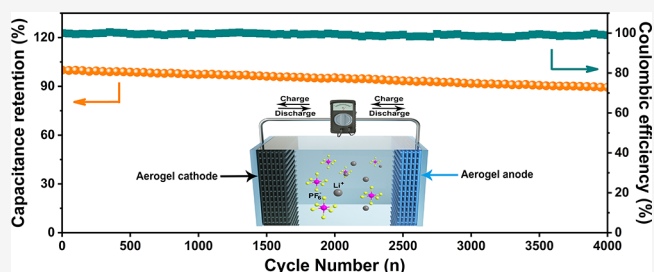


Supporting Information

ABSTRACT: Two-dimensional conductive metal–organic frameworks (2D CMOFs) can be regarded as high-performance electrode substances owing to their rich hierarchical porous architecture and excellent electrical conductivity. However, the sluggish kinetics behavior of electrodes within the bulk structure restricts their advances in energy storage fields. Herein, a series of graphene-based mixed-dimensional composite aerogels are achieved by incorporating the 2D M-tetrahydroxy-1,4-quinone (M-THQ) (M = Cu, Cu/Co, or Cu/Ni) into CNTs@rGO aerogel electrodes using a 3D-printing direct ink writing (DIW) technique.

Benefiting from the high capacity of M-THQ and abundant porosity of the 3D-printed microlattice electrodes, an excellent capacitive performance of the M-THQ@CNTs@rGO cathodes is achieved based on the fast electron/ion transport. Furthermore, the 3D-printed lithium-ion hybrid supercapacitor (LIHCs) device assembled with Cu/Co-THQ@CNTs@rGO cathode and C60@VNNWs@rGO anode delivers a remarkable electrochemical performance. More importantly, this work manifests the practicability of printing 2D CMOFs electrodes, which provides a substantial research basis for 3D printing energy storage.

KEYWORDS: Additive manufacturing, 3D printing, Two-dimensional conductive metal–organic framework, Lithium-ion hybrid supercapacitors, Energy storage device



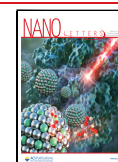
Lithium ion hybrid supercapacitors (LIHCs) have been widely utilized in various energy storage systems due to their high energy/power density, fast charge/discharge capability, and excellent cyclic stability.^{1–3} Generally, transition metal compounds have been employed as the cathodes of LIHCs, while the low gravimetric capacity (<200 mAh g⁻¹) and poor electrical conductivity have considerably restricted their progress in energy storage fields.^{4,5} Thus, it is crucial to probe more compatible cathode materials with higher capacity to improve the electrochemical property of the LIHCs. Two-dimensional CMOFs embrace the extended π -conjugated and porous graphene-like structures, which have recently drawn considerable attention because of their high electrical conductivity, large specific surface areas and porosity, and the adjustable chemical composition.⁶ The large porosity of 2D CMOFs facilitates ion transportation and electrolyte penetration to a great extent.^{6,7} Additionally, the redox-active organic bridging ligands with the active sites and various valences of metal ions/clusters are beneficial for enhancing pseudocapacitance. Therefore, these advantages make 2D CMOFs an emerging candidate for application in electrochemical energy storage systems with excellent electrochemical performance.

The 2D copper-benzoquinoid-based metal–organic framework (e.g., 2D Cu-based THQ) is a promising cathode material based on its porosity and semiconducting features, which are beneficial to charge transport and energy storage.^{8–11} In addition, considering that copper is naturally plentiful in the earth's crust, and the organic linkers of 2D Cu-based THQ can also be derived from the natural resources.⁸ However, it is prone to aggregation, which may decrease the electrochemical performance of the electrodes and restrict their development in scalable energy storage systems. As an advanced manufacturing technology, 3D-printing direct ink writing (DIW) technology can construct a 3D periodic microlattice architecture with low density, high porosity, and adjustable electrical conductivity, which facilitates the diffusion of electrolyte ions and further boosts the electrochemical performance of electrode materials.^{12–17} Therefore, our

Received: November 11, 2021

Revised: January 22, 2022

Published: January 26, 2022



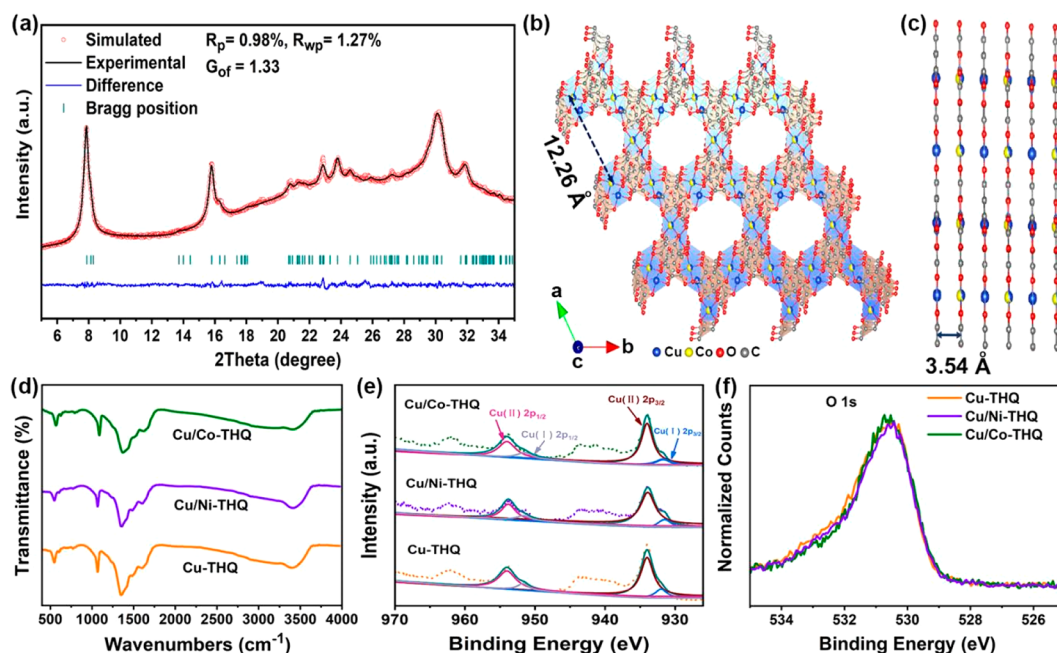


Figure 1. (a) PXRD pattern of Cu/Co-THQ. (b) Graphic representation of Cu/Co-THQ. (c) Unit-cell structure of Cu/Co-THQ. (d) FTIR of Cu-THQ, Cu/Co-THQ, and Cu/Ni-THQ ligands in solid state. XPS spectra of (e) Cu 2p and (f) O 1s of Cu-THQ, Cu/Co-THQ, and Cu/Ni-THQ.

strategy is introducing the 2D Cu-based THQ into 3D-printed periodic microlattice electrode including carbon nanotubes (CNTs) and reduced graphene oxide (rGO) with higher conductivity, which can be expected to enhance the electrochemical property of the electrodes.

Herein, we strategically constructed a series of graphene-based mixed-dimensional hybrid aerogel electrodes with periodic microlattices by employing a software-controlled 3D-printing DIW technology. In these electrodes, the viscous pseudoplastic positive electrode's nanocomposite ink is composed of M-THQ, CNTs and rGO, while that of the negative electrode consists of the fullerene (C60), VN nanowires (VNNWs), and rGO. In these microlattices, M-THQ, VNNWs, and rGO yield high capacitance, which combined with thick electrode architectures with high specific surface area, resulting in a high energy density. Moreover, the high electrical conductivity of CNTs and rGO enables a fast charge transfer within the thick electrode, enhancing the electrochemical property of the electrodes. Furthermore, the M-THQ and C60 can be served as the "lubricant" between the rGO layers, modifying the partial structural deformation (Figure S1). Moreover, the porous structures with periodic microlattices are constructed from mixed-dimensional components, maintaining structural stability under a certain extent of deformation. Regarding the charge balance between the Cu/Co-THQ@CNTs@rGO aerogel cathode and C60@VNNWs@rGO aerogel anode, the assembled LIHCs device delivers a high operating voltage of 4 V, a maximum gravimetric specific capacity of 178.68 F g⁻¹ and gravimetric energy density of 396.89 Wh kg⁻¹. Therefore, the strategy of constructing multidimensional architectures provides an effective approach for the next-generation scalable energy storage devices.

The 2D Cu-THQ, Cu/Co-THQ (Cu/Co = 39:61), and Cu/Ni-THQ (Cu/Ni = 43:57) were synthesized by a kinetically controlled synthesis process, and the specific

statements are provided in Supporting Information (SI). The field-emission scanning electron microscopy (FESEM) and the high-resolution transmission electron microscope (HRTEM) images clearly reveal the morphology and microstructures of 2D Cu-THQ, Cu/Co-THQ and Cu/Ni-THQ with the crystallite sizes are around 10–30 nm (Figure S2a–f). All of the hexagonal pores of 2D Cu-THQ, Cu/Co-THQ, and Cu/Ni-THQ are ~1.2 nm, corresponding to the expected structure and powder X-ray diffraction (PXRD) pattern (Figure 1a–c, Figure S3c–f), and the crystalline structures of Cu-THQ, Cu/Co-THQ, and Cu/Ni-THQ agree well with their standard Kagome lattice and reported PXRD patterns of Cu-THQ (Figure 1a, Figure S3a,b), which manifests the formation of M-THQ.⁸ Rietveld refinements of M-THQ (green line in Figure 1a and Figure S3a,b) demonstrate that the unit cell ascribes to *Cmcm* space group, which is consistent with agreement with the previous reports.⁹ The Fourier transform infrared (FTIR) spectra (Figure 1d) of Cu-THQ, Cu/Co-THQ, and Cu/Ni-THQ exhibit that the absorption features at 3350 and 1700 cm⁻¹ correspond to C–O and C=O stretching modes, respectively.¹⁰ Additionally, a wide band at 3000 cm⁻¹ was discovered in FTIR spectra of the above-mentioned ink materials, which is in accordance with the NH stretching modes of ethylenediamine molecules within the CMOFs for charge balancing.¹¹ X-ray photoelectron spectroscopy (XPS) spectra demonstrate that a mixed valence state of Cu centered is presented in all of the M-THQ (Figure 1e), which agrees well with the previous report.⁸ Furthermore, O 1s XPS spectra (Figure 1f) exhibits the binding energy of the O 1s electron increases when changing the metal atom in THQ from Cu (530.53 eV) to Cu/Co (530.67 eV), indicating that outer electron density on the O–M–O motif reduced with the introduction of Co atoms.

The proper shear-thinning and viscoelastic response rheological behaviors of ink are very important for direct-writing 3D printing. As shown in Figure 2b, the Cu/Co-

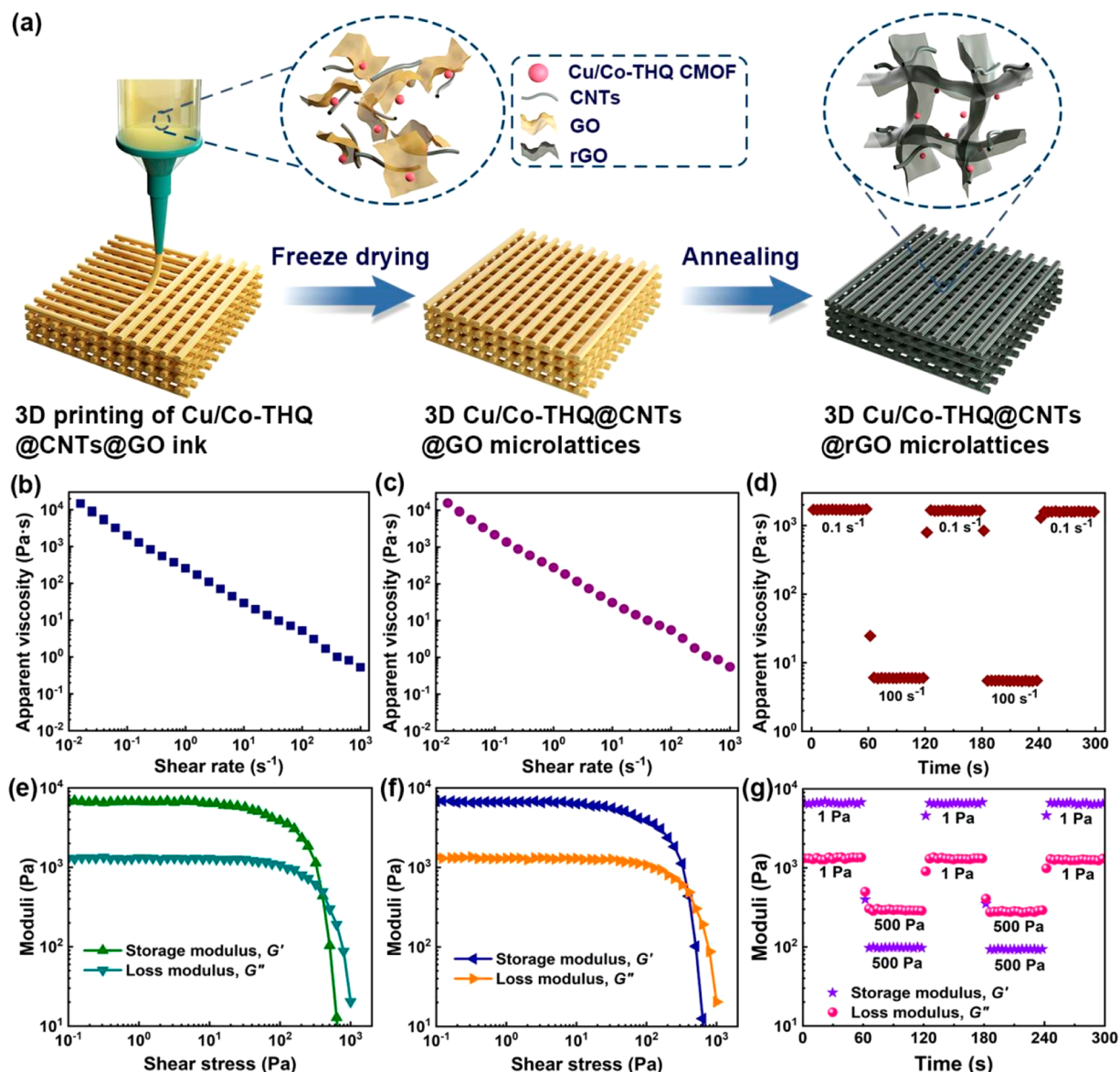


Figure 2. (a) Schematic diagram of the as-fabricated microlattices. Rheological properties of Cu/Co-THQ@CNTs@GO slurry inks. (b) The relationship between the apparent viscosity and shear rate for inks. (c) The relationship between the storage modulus (G') and loss modulus (G'') and the shear stress for inks. (d,e) The relationship between the apparent viscosity and the shear rate for inks, and storage modulus (G') and loss modulus (G'') and the shear stress for inks after 4 weeks of storage. (f,g) Cyclic shear-thinning experiment of the as-fabricated ink exhibiting viscosity, storage (G'), and loss (G'') modulus response.

THQ@CNTs@GO ink is non-Newtonian fluid with significant shear-thinning behavior, which would facilitate ink extrusion and maintain print shape. Figure 2c exhibits the storage modulus (G') and loss modulus (G'') of the Cu/Co-THQ@CNTs@GO ink. When the shear stress is low at the range of 10^{-1} to 10^2 Pa, which corresponds to the state of ink after a complete printing without any external forces, the G' is several times larger than G'' , indicating the solid-state behavior of the ink. At the right end of the curve, where the shear stress is greater than 10^2 Pa, both G' and G'' start to decrease while G' is decreasing at a greater rate than G'' when the shear stress increases (representing the ink is being extruded), which suggests that the viscosity of the ink begins to surpass the elasticity, demonstrating a liquid-like behavior. This representative shear-thinning behavior demonstrates the good flow and vertical accumulation of the Cu/Co-THQ@CNTs@GO ink.

Moreover, the ink also demonstrated an excellent stability with no obvious change after 30 days (Figure 2d,e). The viscosity and moduli's cyclic changes are shown in Figure 2f,g to investigate the transient response and stability of the Cu/Co-THQ@CNTs@GO ink. The ink is subject to three cycles of low/high shear rate for 60 s, respectively. The viscosity of the as-fabricated ink suddenly drops to below 6.6 Pa·s from ~ 1800 Pa·s when the shear rate is increased to 100 times (from 0.1 to 100 s^{-1}) and is still stable for each cyclic test. The moduli also exhibit a similar changing trend with the viscosity when the shear stress suddenly increases or decreases (Figure 2g). The inks exhibit minimal mechanical hysteresis during circulation, which may be due to the initial disequilibrium.¹⁸ All of the results strongly demonstrate the outstanding printing performance of the Cu/Co-THQ@CNTs@GO ink. In addition, Cu-THQ@CNTs@GO, Cu/Ni-THQ@CNTs@GO, and C60@

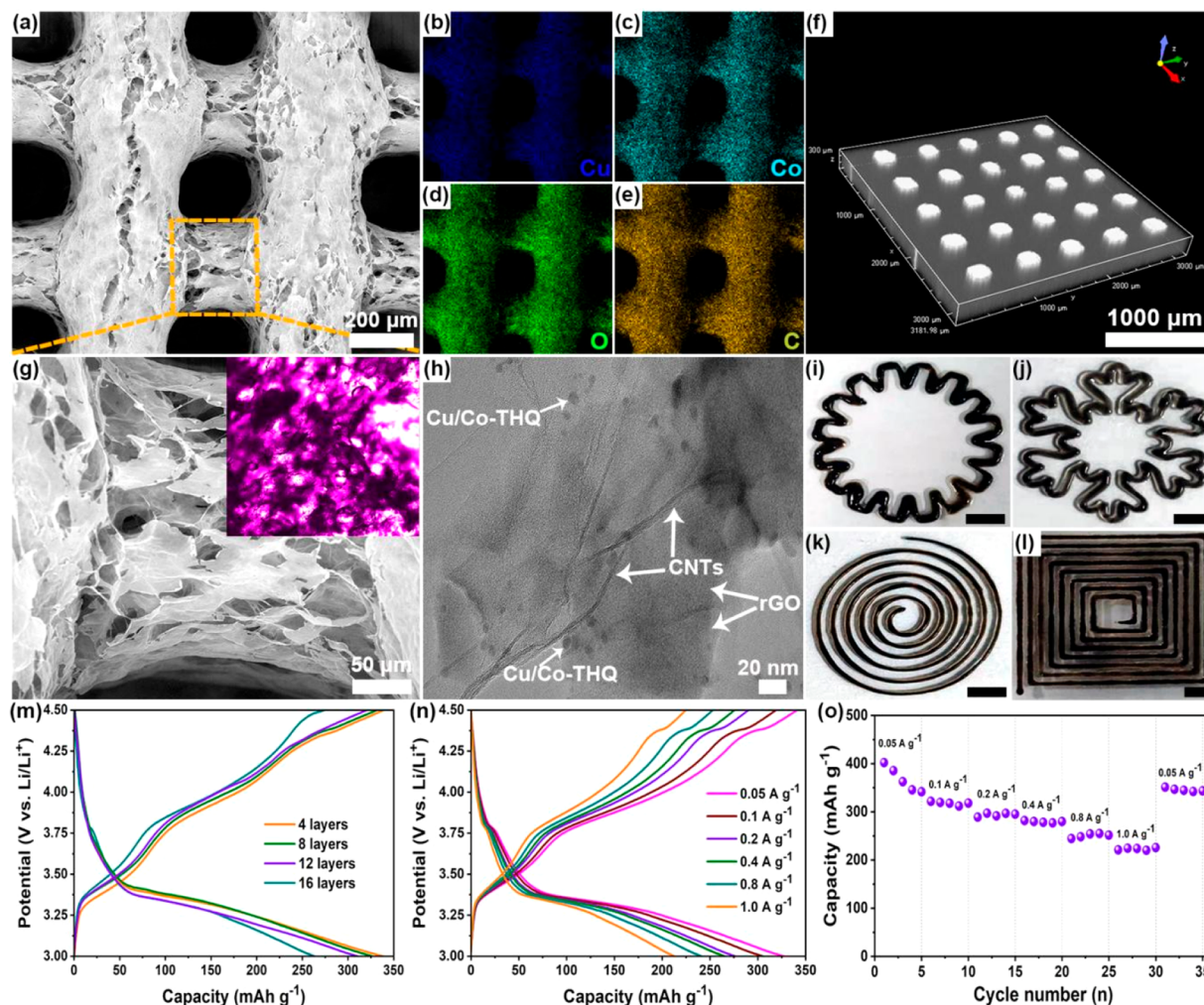


Figure 3. (a) SEM image, (b–e) EDX images of Cu, Co, O, and C elements in (a), (f) LCSM image of the as-printed Cu/Co-THQ@CNTs@rGO microlattices electrode and its gradient porous structure. (g) Magnified image from a cylindrical rod in (a), inset shows its porous structure. (h) TEM images of the printed Cu/Co-THQ@CNTs@rGO microlattices electrode. (i–l) Photographs of the 3D-printed Cu/Co-THQ@CNTs@rGO architectures with multifarious patterns. Scale bars, 2 mm. Electrochemical performance of the printed Cu/Co-THQ@CNTs@rGO electrode. (m) The typical charging/discharging curves of printed microlattices electrodes with various layers with the operating potential window from 3.0 to 4.5 V (vs Li/Li⁺) at 0.05 A g⁻¹. (n) The charging/discharging curves of the printed microlattices electrodes with 12 layers at the current densities of 50–1000 mA g⁻¹. (o) Rate capability of the 3D-printed electrodes with 12 layers at the different current densities ranging from 0.05 to 1.0 A g⁻¹.

VNNWs@GO inks exhibited similar behaviors (Figure S4, Figure S5, and Figure S6). The fabrication process of 3D-printed M-THQ@CNTs@rGO microlattices is illustrated in Figure 2a. The 3D M-THQ@CNTs@rGO microlattices were printed via DIW technology using a homogeneous ink containing a mixture of M-THQ, CNTs, and GO suspension. The printed architectures were then freeze-dried to obtain aerogels, and then annealed under Ar atmosphere to convert GO to rGO. Indeed, the fabrication strategy of 3D C60@VNNWs@rGO microlattice is consistent with that of M-THQ@CNTs@rGO. In the C60@VNNWs@rGO microlattice anode, the VNNWs with porous structure shows a high theoretical capacity, promoting the electrochemical performance (Figure S7).⁵ The 3D-printed M-THQ@CNTs@rGO microlattice cathode and C60@VNNWs@rGO microlattice anode both demonstrate multiple orthogonal layers of parallel porous cylindrical rods (Figure 3a, Figure S8a, Figure S9a, and Figure S10a) in which the diameter of the porous cylindrical rod and center-to-center rod spacing are ~250 and 600 μm, respectively. Energy dispersive X-ray

spectroscopy (EDX) images of the 3D Cu/Co-THQ@CNTs@rGO microlattices exhibit that Cu, Co, O, and C are homogeneously distributed in the whole microlattice (Figure 3b–e), demonstrating the formation of Cu/Co-THQ@CNTs@rGO electrode. Furthermore, the laser confocal scanning microscopy (LCSM) image demonstrates that the as-prepared electrode possesses an orderly channel structure (Figure 3f). The high-magnification SEM and LCSM images (Figure 3g and its inset) exhibit the 3D-printed Cu/Co-THQ@CNTs@rGO architecture with an interconnected porous network structure, which consists of Cu/Co-THQ, CNTs and randomly oriented rGO (Figure 3h). Moreover, the homogeneous Cu/Co-THQ@CNTs@rGO ink with high viscosity and optimum elasticity was printed to form various patterns with high precision (Figure S11 and Figure 3i–l). Indeed, the EDX images confirm the formation of C60@VNNWs@rGO microlattice anode (Figure S10c–f). The 3D-printed Cu-THQ@CNTs@rGO, Cu/Ni-THQ@CNTs@rGO, and C60@VNNWs@rGO architectures also achieve the

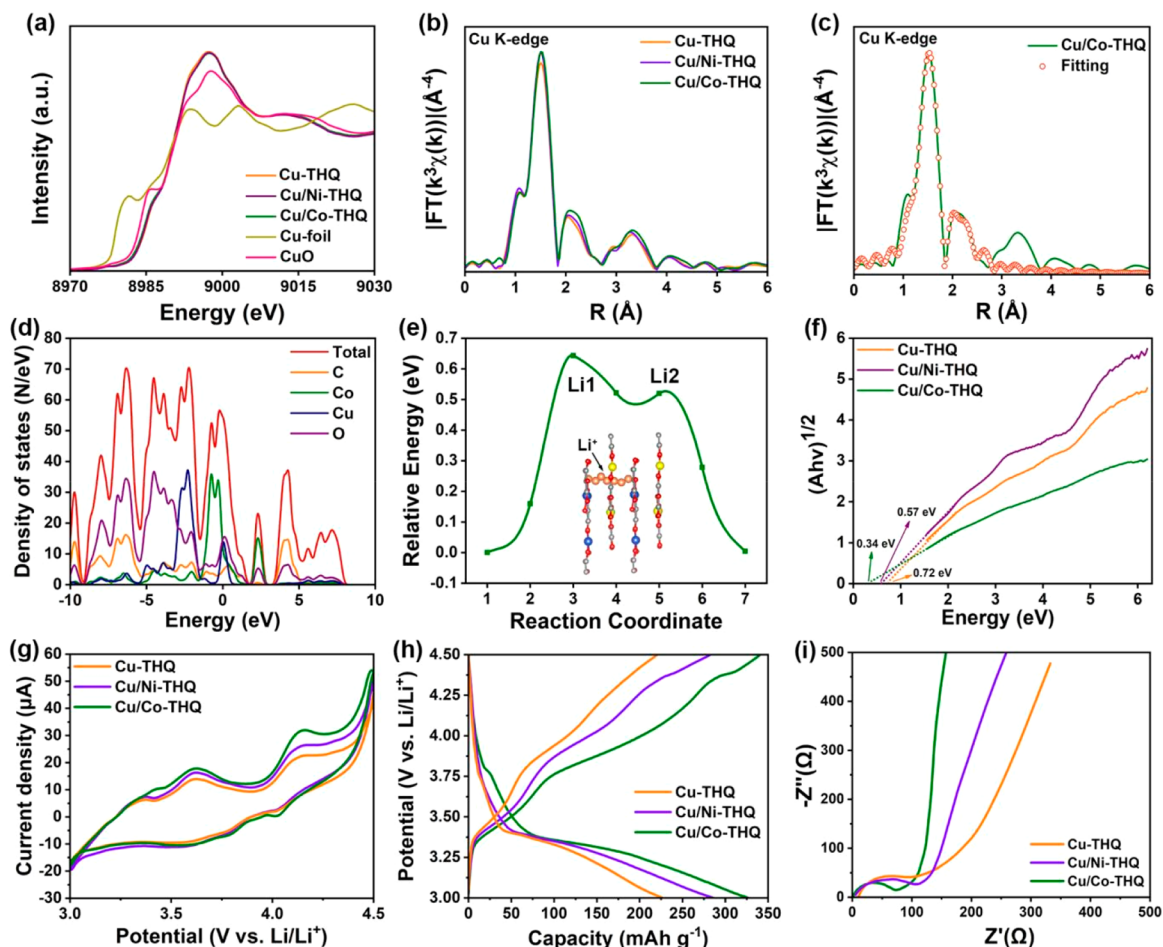


Figure 4. (a) Cu K-edge XANES spectra, and (b) corresponding Fourier transforms of k^3 -weighted EXAFS spectra for Cu-THQ, Cu/Ni-THQ, and Cu/Co-THQ and references. (c) The typical fitting curve of the EXAFS signal in k -space for Cu/Co-THQ. (d) Density of state for Cu/Co-THQ. (e) Energy barrier profile of Li^+ migration in Cu/Co-THQ, inset is the corresponding migration process. (f) Estimated bands of Cu-THQ, Cu/Ni-THQ, and Cu/Co-THQ. Electrochemical performance of M-THQ@CNTs@rGO microlattice electrodes that are 12 layers thick (M = Cu, Cu/Co, and Cu/Ni). (g) CV curves at the scan rate of 0.5 mV s^{-1} . (h) The typical charging/discharging curves with the operating potential window ranging from 3.0 to 4.5 V (vs Li/Li^+) at the current density of 0.05 A g^{-1} . (i) Nyquist plots.

interconnected porous network structure (Figure S8b,c, Figure S9b,c, and Figure S10b,g,h).

Furthermore, electrochemical performances of Cu-THQ@CNTs@rGO, Cu/Co-THQ@CNTs@rGO, and Cu/Ni-THQ@CNTs@rGO microlattice cathodes were investigated in a two-electrode system. Benefiting from the high specific surface areas of Cu-THQ@CNTs@rGO, Cu/Co-THQ@CNTs@rGO, and Cu/Ni-THQ@CNTs@rGO microlattices (Figure S8d, Figure S9d, and Figure S12), the 3D-printed Cu/Co-THQ@CNTs@rGO electrode with four layers achieved a high specific capacity of $338.19 \text{ mAh g}^{-1}$ at 100 mA g^{-1} . The 3D-printed Cu/Co-THQ@CNTs@rGO with 8 and 12 layers shows a similar gravimetric capacity with 4 layers (332.18 and $325.44 \text{ mAh g}^{-1}$, respectively), which demonstrates that ion diffusion continues to not restrict the capacitive performance even in the 12 layers thick electrode (Figure 3m). Additionally, the 3D-printed electrode with 16 layers thick yields a low capacity due to the long electron transfer path (Figure 3m). To realize the feasibility and practicability of the printing microlattice cathode, the Cu/Co-THQ@CNTs@rGO electrode with 12 layers is selected. Figure 3no, Figure S13, Figure S14, and Figure S15 indicate that the 3D-printed Cu/Co-THQ@CNTs@rGO electrode delivers an excellent rate and

cycling performance, low electrical resistance, and high reversibility. Moreover, the electrochemical performance of the C60@VNNWs@rGO microlattice anode was investigated (Figure S16), the specific details are provided in the SI.

The X-ray absorption spectroscopy measurements were carried out to explore the local structural information for Cu, Co, and Ni. Figure 4a shows The X-ray absorption near-edge structure (XANES) spectra of Cu-THQ, Cu/Co-THQ, and Cu/Ni-THQ at Cu K-edge are exhibited in Figure 4a, and they are similar to that of CuO reference rather than the Cu foil reference, demonstrating that the valence of Cu in Cu-THQ, Cu/Co-THQ, and Cu/Ni-THQ is +2.⁸ Moreover, the doping of Co or Ni element is not able to cause any changes in the local structure of copper atoms as well as the formation of alloys or distortions in the as-prepared Cu/Co-THQ and Cu/Ni-THQ samples. In addition, the magnified Cu K-edge XANES curves (Figure S17a) demonstrate the near-edge absorption energy of Cu/Ni-THQ located between Cu/Co-THQ and Cu-THQ, which demonstrates that the average electron density of Cu in Cu/Ni-THQ is higher and lower than that in Cu-THQ and Cu/Co-THQ, respectively. Figure S17b,c displays the XANES spectra of Cu/Ni-THQ at Ni K-edge and Cu/Co-THQ at Co K-edge, respectively. Cu/Ni-

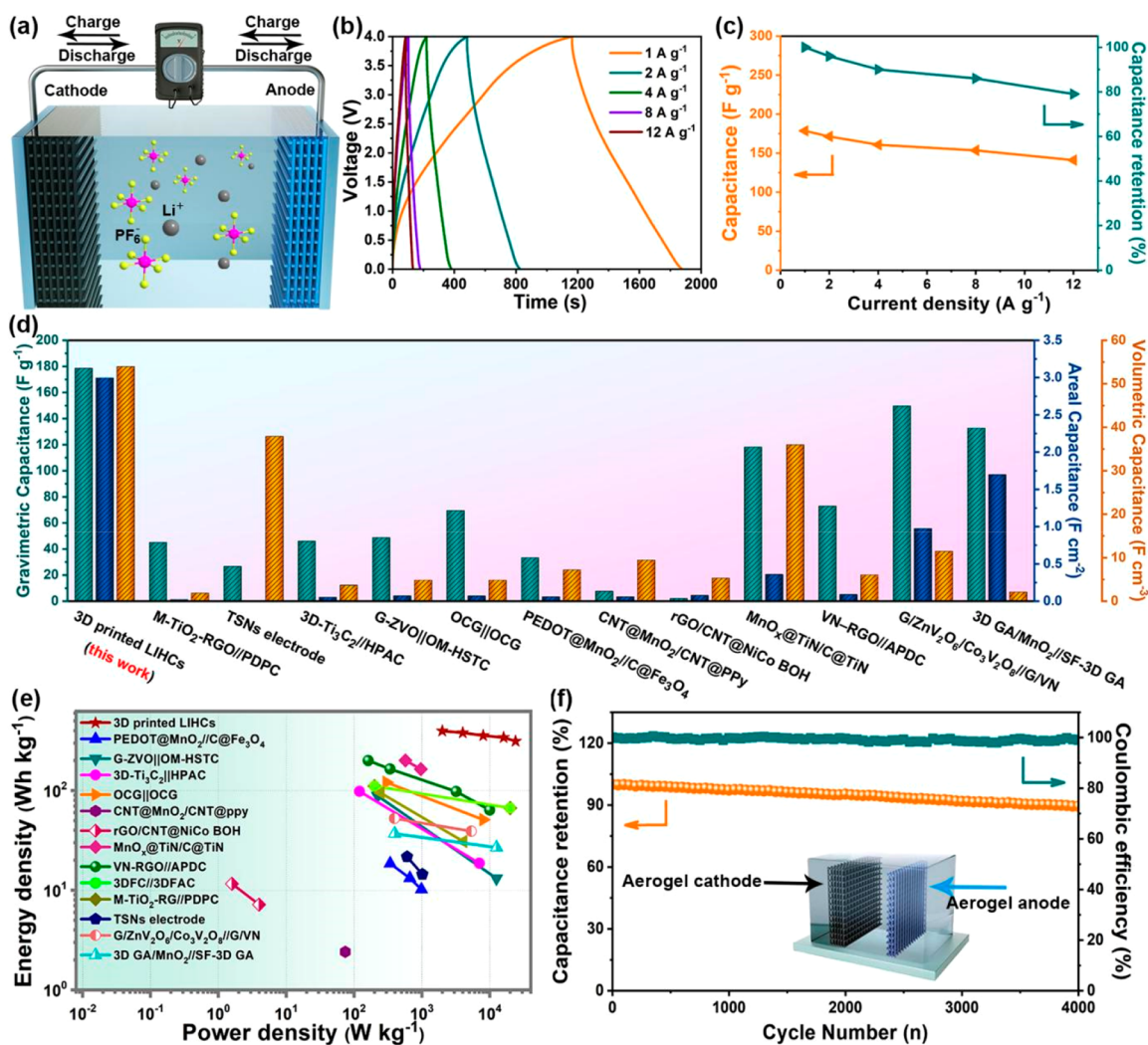


Figure 5. (a) Working principle and schematic diagram of the 3D-printed LHCs device. (b) GCD curves. (c) Rate capability. (d) Comparison of electrochemical performance of this 3D-printed LHCs device with previous electrochemical energy storage devices.^{5,12,16,25–33} (e) Ragone plot (power density versus energy density).^{5,12,16,25–34} (f) The capacity retention and CE after 4000 cycles.

THQ exhibits similar XANES spectra with those of NiO reference, which proves the valence of Ni in Cu/Ni-THQ is +2. Indeed, the XANES spectra of Cu/Co-THQ sample is similar to those of metal oxides references and different from Co foil. The Fourier transform extended X-ray absorption fine structure (EXAFS) spectras of Cu-THQ, Cu/Co-THQ, and Cu/Ni-THQ are illustrated in Figure 4b. Apparently, the spectras of both Cu/Co-THQ and Cu/Ni-THQ are similar to those of Cu-THQ. It can be observed that these samples exhibited one conspicuous Fourier transform peak at 1.55 Å belongs to the scattering of Cu–N/O coordination. Moreover, a shoulder peak at 2.13 Å was also detected and attributed to Cu–C scattering. Furthermore, the EXAFS data of Cu-THQ, Cu/Co-THQ, and Cu/Ni-THQ at Cu K-edge were fitted via the Artemis software (Figure 4c and Figure S18a,b) to collect more detailed structural parameters (Table S1). The fitting curves of Cu-THQ, Cu/Co-THQ, and Cu/Ni-THQ corresponded well with the experimental spectra, revealing that the doped Co and Ni have no obvious effect on the pristine Cu-THQ structure. According to the coordination number of Cu–O in Table S1, the simulated EXAFS spectra of all three samples are based on Cu–O4 model. The main Fourier transform peaks of Cu/Ni-THQ at Ni K-edge (Figure S18c)

and Cu/Co-THQ at Co K-edge (Figure S18d) and their EXAFS structural parameters were further investigated (Table S2 and Table S3). The fitting curves of both Cu/Ni-THQ and Cu/Co-THQ are consistent with their experimental spectra, which represents that no Ni or Co cluster is formed after the doping process. For the Cu/Co-THQ, the coordination number of Co–O is 4.4 (Table S2), which means that there are four oxygen atoms around a cobalt atom. Similar results can be found in Cu/Ni-THQ (Table S3). For more clarification regarding the coordination structures in Cu-THQ, Cu/Ni-THQ, and Cu/Co-THQ, high-resolution wavelet transform (WT) in both k and R spaces of Cu K-edge EXAFS oscillation was further investigated, as shown in Figure S19. Compared with the WT signals of Cu foil, no Cu–Cu coordination was detected in Cu-THQ, Cu/Ni-THQ, and Cu/Co-THQ. Moreover, one maximum intensity at 4.5 Å^{−1} can be observed for Cu-THQ, Cu/Ni-THQ, and Cu/Co-THQ, which is consistent with the CuO reference. Similar results were achieved in the WT plots of Cu/Ni-THQ at Ni K-edge (Figure S18e) and Cu/Co-MOF at Co K-edge (Figure S18f), which further identifies the isolated feature of Cu, Co, and Ni species in the as-prepared Cu-THQ, Cu/Co-THQ, and Cu/Ni-THQ.

Density functional theory (DFT) calculations were also performed to deepen the understanding about the process of improvement in electrochemical performance of Cu/Co-THQ. Density of states (DOS) plots of Cu-THQ, Cu/Co-THQ, and Cu/Ni-THQ are demonstrated in Figure 4d and Figure S20a,b, respectively. Evidently, no band gap at 0 eV can be observed, revealing that all Cu-THQ, Cu/Co-THQ, and Cu/Ni-THQ show metallic properties. Meanwhile, there is a conspicuous band gap at 2.5 eV in Cu-THQ and Cu/Ni-THQ, which indicates that Cu/Co-THQ possesses more empty states for electrons, and consequently higher electronic conductivity (Table S4).¹⁹ In addition, the Li⁺ migration through Cu-THQ, CuCo-MOF, and CuNi-MOF was surveyed by climbing-image nudged elastic band (CI-NEB) methods.^{20,21} The calculated energy barrier of Li-ion migration for three THQs is shown in Figure 4e and Figure S20c,d. The inset of these figures displays the corresponding migration process, containing seven Li ions which represent the whole path. Two asymmetric peaks appear in the process of Li⁺ migration because the surrounding ion environment of Li ions that migrated from layer A to layer B (Li1) is different from those that migrated from layer B to layer A (Li2).^{22–24} The corresponding Li⁺ diffusion energy barrier at Li1 site for Cu-THQ is much higher than that for Cu/Co-THQ and Cu/Ni-THQ, suggesting that the lowest Li⁺ migration occurs in the pristine Cu-THQ. Furthermore, a lower energy barrier is obtained in Cu/Co-THQ at Li2 site compared with that in Cu/Ni-THQ, which is beneficial for fast reaction kinetics and superior electrochemical properties of Cu/Co-THQ. The smallest bandgap of the Cu/Co-THQ is demonstrated by UV-vis spectra (Figure 4f), which is calculated to be ~0.34 eV, much lower than that for the Cu-THQ (0.72 eV) and Cu/Ni-THQ (0.57 eV). This result matches well with the DFT results. Therefore, the Cu/Co-THQ@CNTs@rGO microlattice in all of the M-THQ@CNTs@rGO microlattice cathode 12 layers thick achieves the best electrochemical performance according to the X-ray absorption fine structure (XAFS) spectrum and experimental results (Figure 4g–i).

The 3D-printed LIHCs device is composed of 3D-printed Cu/Co-THQ@CNTs@rGO cathode, C60@VNNWs@rGO anode, and LiPF₆/EC/DMC liquid electrolyte (Figure 5a, Figure S21). Cyclic voltammetry (CV) carried out on the 3D-printed LIHCs device between 0 and 4.0 V is exhibited in Figure S22a, demonstrating an excellent reversibility. Figure 5b exhibits the charging/discharging curves of the 3D-printed LIHCs device at the different current densities of 1–12 A g⁻¹ in a two-electrode configuration. The large specific capacity of 178.68 F g⁻¹ and symmetric triangular-like GCD curves (Figure 5b,c) demonstrate that the 3D-printed LIHCs deliver a fine capacitive behavior and rate capability. Additionally, the 3D-printed LIHC device yields an excellent areal specific capacitance of 2.99 F cm⁻² and volumetric specific capacitance of 53.98 F cm⁻³. These values have exceeded those of previously reported electrochemical energy storage systems (Figure 5d), such as M-TiO₂-RG//PDPC,²⁵ TSNs electrode,²⁶ 3D-Ti₃C₂//HPAC,²⁷ G-ZVO//IOM-HSTC,²⁸ OCG//OCG,²⁹ PEDOT@MnO₂//C@Fe₃O₄,³⁰ CNT@MnO₂/CNT@PPy,³¹ rGO/CNT@NiCo BOH,³² MnO_x@TiN/C@TiN,³³ VN-RGO//APDC,⁵ G/ZnV₂O₆/Co₃V₂O₈//G/VN,¹² and 3D GA/MnO₂//SF-3D GA.¹⁶ Meanwhile, the relatively low electrical resistance of the as-printed LIHCs demonstrates its excellent electrochemical performance (Figure S22b). Ragone plots of the 3D-printed LIHCs show a high gravimetric energy

density of 396.89 Wh kg⁻¹ at the gravimetric power density of 1999.90 W kg⁻¹, depict a gravimetric energy density of 313.56 Wh kg⁻¹ at a ultrahigh gravimetric power density of 24002.04 W kg⁻¹ (Figure 5e), which surpasses the most advanced energy storage devices reported previously,^{5,12,16,25–34} and further confirm the excellent electrochemical property of the printed LIHCs device. Moreover, the printed LIHC device achieves an impressive cycle performance with a capacity retention of 89.43% after 4000 charging/discharging cycles at 2 A g⁻¹ and a Coulombic efficiency (CE) of nearly 100% (Figure 5f).

In summary, a series of graphene-based mixed-dimensional hybrid aerogel electrodes were synthesized by utilizing the software-controlled 3D printing DIW technique. These hybrid aerogel electrodes embrace an engineered porous architecture, which allows a fast electron transport and efficient ion diffusion, thereby yielding an excellent electrochemical performance. Additionally, introducing 2D M-THQ into graphene-based aerogel electrodes led to an outstanding electrochemical performance of 3D printing microlattice electrodes because of their high capacity and “lubricant” function of 2D M-THQ. Benefiting from the rich and hierarchical porous structure of the Cu/Co-THQ @CNTs@rGO aerogel cathode and C60@VNNWs@rGO aerogel anode, the 3D-printed LIHC device achieved a large gravimetric specific capacitance of 178.68 F g⁻¹, excellent gravimetric energy density of 396.89 Wh kg⁻¹, and impressive cyclic stability. Moreover, this work introduces the 2D conductive metal-organic frameworks into 3D-printed aerogel electrodes, which demonstrate a great prospect for the future for more efficient electrochemical energy storage devices.

■ ASSOCIATED CONTENT

Supporting Information

The Supporting Information is available free of charge at <https://pubs.acs.org/doi/10.1021/acs.nanolett.1c04367>.

Experimental section, data analysis description of structural characterization of VN electrode material and electrochemical performance of the C60@VNNWs@rGO microlattice electrode, additional figures and tables (PDF)

■ AUTHOR INFORMATION

Corresponding Authors

Jianhong Peng – Institute of Advanced Electrochemical Energy, Xi'an University of Technology, Xi'an, Shaanxi 710048, P.R. China; Email: pjhjhj@sohu.com

Xifei Li – Institute of Advanced Electrochemical Energy, Xi'an University of Technology, Xi'an, Shaanxi 710048, P.R. China; orcid.org/0000-0002-4828-4183; Email: xfli2011@hotmail.com

Xueliang Sun – Department of Mechanical and Materials Engineering, University of Western Ontario, London, Ontario N6A5B9, Canada; orcid.org/0000-0003-0374-1245; Email: xsun9@uwo.ca

Bingang Xu – Nanotechnology Center, Institute of Textiles and Clothing, The Hong Kong Polytechnic University, Kowloon, Hong Kong 999077, P.R. China; orcid.org/0000-0002-1277-8747; Email: tcxubg@polyu.edu.hk

Authors

Jingxin Zhao – Nanotechnology Center, Institute of Textiles and Clothing, The Hong Kong Polytechnic University, Kowloon, Hong Kong 999077, P.R. China

Yan Zhang – Key Laboratory of Functional Polymer Materials and State Key Laboratory of Medical Chemical Biology, Institute of Polymer Chemistry, College of Chemistry, Nankai University, Tianjin 300071, P.R. China

Hongyu Lu – Institute of Advanced Electrochemical Energy, Xi'an University of Technology, Xi'an, Shaanxi 710048, P.R. China

Yafei Wang – Key Laboratory of Functional Polymer Materials and State Key Laboratory of Medical Chemical Biology, Institute of Polymer Chemistry, College of Chemistry, Nankai University, Tianjin 300071, P.R. China

Xu Dong Liu – Centre of Laser Fusion, China Academy of Engineering Physics, Mianyang 621900, P.R. China

Hirbod Maleki Kheimeh Sari – Institute of Advanced Electrochemical Energy, Xi'an University of Technology, Xi'an, Shaanxi 710048, P.R. China

Shufan Chen – Centre of Laser Fusion, China Academy of Engineering Physics, Mianyang 621900, P.R. China

Yongjun Zhang – Key Laboratory of Functional Polymer Materials and State Key Laboratory of Medical Chemical Biology, Institute of Polymer Chemistry, College of Chemistry, Nankai University, Tianjin 300071, P.R. China;

orcid.org/0000-0002-1079-4137

Complete contact information is available at:

<https://pubs.acs.org/10.1021/acs.nanolett.1c04367>

Author Contributions

[#]J.Z., Y.Z., H.L., and Y.W. contributed equally to this work.

Notes

The authors declare no competing financial interest.

ACKNOWLEDGMENTS

The authors would like to acknowledge the funding supports from the Research Grants Council of Hong Kong (RGC Postdoctoral Fellowship Scheme, Grant PDFS2122-SS03) for the work reported here.

REFERENCES

- (1) Wang, G.; Oswald, S.; Löffler, M.; Müllen, K.; Feng, X. Beyond Activated Carbon: Graphite-Cathode-Derived Li-ion Pseudocapacitors with High Energy and High Power Densities. *Adv. Mater.* **2019**, *31*, 1807712.
- (2) Ou, X.; Zhang, G.; Zhang, S.; Tong, X.; Tang, Y. Simultaneously pre-alloying and artificial solid electrolyte interface towards highly stable aluminum anode for high-performance Li hybrid capacitor. *Energy Storage Mater.* **2020**, *28*, 357–363.
- (3) Baek, D.; Lee, K.; Park, J.; Kim, J.; Lee, J.; Lim, J.; Lee, S.; Shin, T.; Jeong, H.; Son, J.; Kang, S.; Kim, J.; Joo, S. Ordered Mesoporous Carbons with Graphitic Tubular Frameworks by Dual Templating for Efficient Electrocatalysis and Energy Storage. *Angew. Chem., Int. Ed.* **2021**, *60*, 1441–1449.
- (4) Lee, W.; Peng, E.; Li, M.; Huang, X.; Xue, J. Rational design of stable 4 V lithium ion capacitor. *Nano Energy* **2016**, *27*, 202–212.
- (5) Wang, R.; Lang, J.; Zhang, P.; Lin, Z.; Yan, X. Fast and Large Lithium Storage in 3D Porous VN Nanowires-Graphene Composite as a Superior Anode Toward High-Performance Hybrid Supercapacitors. *Adv. Funct. Mater.* **2015**, *25*, 2270–2278.
- (6) Sheberla, D.; Sun, L.; Blood-Forsythe, M.; Er, S.; Wade, C.; Brozek, C.; Aspuru-Guzik, A.; Dincă, M. High Electrical Conductivity in Ni₃(2,3,6,7,10,11-hexamino-triphenylene)₂, a Semiconducting

Metal-Organic Graphene Analogue. *J. Am. Chem. Soc.* **2014**, *136*, 8859–8862.

(7) Chen, G.; Gee, L. B.; Xu, W.; Zhu, Y.; Lezama-Pacheco, J. S.; Huang, Z.; Li, Z.; Babicz, J. T.; Choudhury, S.; Chang, T.-H.; Reed, E.; Solomon, E. I.; Bao, Z. Valence-Dependent Electrical Conductivity in a 3D Tetrahydroxyquinone-Based Metal-Organic Framework. *J. Am. Chem. Soc.* **2020**, *142*, 21243–21248.

(8) Jiang, Q.; Xiong, P.; Liu, J.; Xie, Z.; Wang, Q.; Yang, X.-Q.; Hu, E.; Cao, Y.; Sun, J.; Xu, Y.; Chen, L. A Redox-Active 2D Metal-Organic Framework for Efficient Lithium Storage with Extraordinary High Capacity. *Angew. Chem., Int. Ed.* **2020**, *59*, S273–S277.

(9) Nyakuchena, J.; Ostresh, S.; Streater, D.; Pattengale, B.; Neu, J.; Fiankor, C.; Hu, W.; Kingstein, E.; Zhang, J.; Zhang, X.; Schmuttenmaer, C.; Huang, J. Direct Evidence of Photoinduced Charge Transport Mechanism in 2D Conductive Metal Organic Frameworks. *J. Am. Chem. Soc.* **2020**, *142*, 21050–21058.

(10) Park, J.; Hinckley, A.; Huang, Z.; Feng, D.; Yakovenko, A.; Lee, M.; Chen, S.; Zou, X.; Bao, Z. Synthetic Routes for a 2D Semiconductive Copper Hexahydroxybenzene Metal-Organic Framework. *J. Am. Chem. Soc.* **2018**, *140*, 14533–14537.

(11) Majidi, L.; Ahmadiparidari, A.; Shan, N.; Misal, S.; Kumar, K.; Huang, Z.; Rastegar, S.; Hemmat, Z.; Zou, X.; Zapol, P.; Cabana, J.; Curtiss, L.; Salehi-Khojin, A. 2D Copper Tetrahydroxyquinone Conductive Metal-Organic Framework for Selective CO₂ Electrocatalysis at Low Overpotentials. *Adv. Mater.* **2021**, *33*, 2004393.

(12) Zhao, J.; Zhang, Y.; Zhao, X.; Wang, R.; Xie, J.; Yang, C.; Wang, J.; Zhang, Q.; Li, L.; Lu, C.; Yao, Y. Direct Ink Writing of Adjustable Electrochemical Energy Storage Device with High Gravimetric Energy Densities. *Adv. Funct. Mater.* **2019**, *29*, 1900809.

(13) Yao, B.; Chandrasekaran, S.; Zhang, J.; Xiao, W.; Qian, F.; Zhu, C.; Duoss, E.; Spadaccini, C.; Worsley, M.; Li, Y. Efficient 3D Printed Pseudocapacitive Electrodes with Ultrahigh MnO₂ Loading. *Joule* **2019**, *3*, 459–470.

(14) Zhao, J.; Zhang, Y.; Huang, Y.; Xie, J.; Zhao, X.; Li, C.; Qu, J.; Zhang, Q.; Sun, J.; He, B.; Li, Q.; Lu, C.; Xu, X.; Lu, W.; Li, L.; Yao, Y. 3D Printing Fiber Electrodes for an All-Fiber Integrated Electronic Device via Hybridization of an Asymmetric Supercapacitor and a Temperature Sensor. *Adv. Sci.* **2018**, *5*, 1801114.

(15) Mohammed, A.; Usgaonkar, S.; Kanheerampockil, F.; Karak, S.; Halder, A.; Tharkar, M.; Addicoat, M.; Ajithkumar, T.; Banerjee, R. Connecting Microscopic Structures, Mesoscale Assemblies, and Macroscopic Architectures in 3D-Printed Hierarchical Porous Covalent Organic Framework Foams. *J. Am. Chem. Soc.* **2020**, *142*, 8252–8261.

(16) Yao, B.; Chandrasekaran, S.; Zhang, H.; Ma, A.; Kang, J.; Zhang, L.; Lu, X.; Qian, F.; Zhu, C.; Duoss, E.; Spadaccini, C.; Worsley, M.; Li, Y. 3D-Printed Structure Boosts the Kinetics and Intrinsic Capacitance of Pseudocapacitive Graphene Aerogels. *Adv. Mater.* **2020**, *32*, 1906652.

(17) Zhao, J.; Zhang, Y.; Huang, Y.; Zhao, X.; Shi, Y.; Qu, J.; Yang, C.; Xie, J.; Wang, J.; Li, L.; Yan, Q.; Hou, S.; Lu, C.; Xu, X.; Yao, Y. Duplex printing of all-in-one integrated electronic devices for temperature monitoring. *J. Mater. Chem. A* **2019**, *7*, 972–978.

(18) Zhang, M.; Vora, A.; Han, W.; Wojtecki, R. J.; Maune, H.; Le, A. B. A.; Thompson, L. E.; McClelland, G. M.; Ribet, F.; Engler, A. C.; Nelson, A. Dual-Responsive Hydrogels for Direct-Write 3D Printing. *Macromolecules* **2015**, *48*, 6482–6488.

(19) Lu, J.; Jung Lee, Y.; Luo, X.; Chun Lau, K.; Asadi, M.; Wang, H.-H.; Brombosz, S.; Wen, J.; Zhai, D.; Chen, Z.; Miller, D. J.; Sub Jeong, Y.; Park, J.-B.; Zak Fang, Z.; Kumar, B.; Salehi-Khojin, A.; Sun, Y.-K.; Curtiss, L. A.; Amine, K. A lithium-oxygen battery based on lithium superoxide. *Nature* **2016**, *529*, 377–382.

(20) Liu, H.; Zhu, Z.; Yan, Q.; Yu, S.; He, X.; Chen, Y.; Zhang, R.; Ma, L.; Liu, T.; Li, M.; Lin, R.; Chen, Y.; Li, Y.; Xing, X.; Choi, Y.; Gao, L.; Cho, H.; An, K.; Feng, J.; Kostecki, R.; Amine, K.; Wu, T.; Lu, J.; Xin, H.; Ong, S.; Liu, P. A disordered rock salt anode for fast-charging lithium-ion batteries. *Nature* **2020**, *585*, 63–67.

(21) Chang, J.; Shang, J.; Sun, Y.; Ono, L.; Wang, D.; Ma, Z.; Huang, Q.; Chen, D.; Liu, G.; Cui, Y.; Qi, Y.; Zheng, Z. Flexible and stable

high-energy lithium-sulfur full batteries with only 100% oversized lithium. *Nat. Commun.* **2018**, *9*, 4480.

(22) Xu, S.-M.; Liang, X.; Wu, X.-Y.; Zhao, S.-L.; Chen, J.; Wang, K.-X.; Chen, J.-S. Multistaged discharge constructing heterostructure with enhanced solid-solution behavior for long-life lithium-oxygen batteries. *Nat. Commun.* **2019**, *10*, 5810.

(23) Jiang, H.; Lu, Z.; Wu, M.; Ciucci, F.; Zhao, T. Borophene: A promising anode material offering high specific capacity and high rate capability for lithium-ion batteries. *Nano Energy* **2016**, *23*, 97–104.

(24) Xu, Z.; Chen, X.; Chen, R.; Li, X.; Zhu, H. Anion charge and lattice volume dependent lithium ion migration in compounds with fcc anion sublattices. *NPJ. Comput. Mater.* **2020**, *6*, 47.

(25) Wang, R.; Wang, S.; Zhang, Y.; Jin, D.; Tao, X.; Zhang, L. Graphene-coupled Ti_3C_2 MXenes-derived TiO_2 mesostructure: promising sodium-ion capacitor anode with fast ion storage and long-term cycling. *J. Mater. Chem. A* **2018**, *6*, 1017–1027.

(26) Gao, R.; Tang, J.; Yu, X.; Lin, S.; Zhang, K.; Qin, L.-C. Layered Silicon-Based Nanosheets as Electrode for 4 V High-Performance Supercapacitor. *Adv. Funct. Mater.* **2020**, *30*, 2002200.

(27) Fang, Y.-Z.; Hu, R.; Zhu, K.; Ye, K.; Yan, J.; Wang, G.; Cao, D. Aggregation-Resistant 3D $\text{Ti}_3\text{C}_2\text{T}_x$ MXene with Enhanced Kinetics for Potassium Ion Hybrid Capacitors. *Adv. Funct. Mater.* **2020**, *30*, 2005663.

(28) Huang, H.; Kundu, D.; Yan, R.; Tervoot, E.; Chen, X.; Pan, L.; Oschatz, M.; Antonietti, M.; Niederberger, M. Fast Na-Ion Intercalation in Zinc Vanadate for High-Performance Na-Ion Hybrid Capacitor. *Adv. Energy Mater.* **2018**, *8*, 1802800.

(29) Dong, S.; Xu, Y.; Wu, L.; Dou, H.; Zhang, X. Surface-functionalized graphene-based quasi-solid-state Na-ion hybrid capacitors with excellent performance. *Energy Storage Mater.* **2018**, *11*, 8–15.

(30) Sun, J.; Huang, Y.; Fu, C.; Huang, Y.; Zhua, M.; Tao, X.; Zhi, C.; Hu, H. A high performance fiber-shaped PEDOT@ MnO_2 /C@ Fe_3O_4 asymmetric supercapacitor for wearable electronics. *J. Mater. Chem. A* **2016**, *4*, 14877–14883.

(31) Yu, J.; Lu, W.; Smith, J.; Booksh, K.; Meng, L.; Huang, Y.; Li, Q.; Byun, J.-H.; Oh, Y.; Yan, Y.; Chou, T.-W. A High Performance Stretchable Asymmetric Fiber-Shaped Supercapacitor with a Core-Sheath Helical Structure. *Adv. Energy Mater.* **2017**, *7*, 1600976.

(32) Liu, M.; Cong, Z.; Pu, X.; Guo, W.; Liu, T.; Li, M.; Zhang, Y.; Hu, W.; Wang, Z. High-Energy Asymmetric Supercapacitor Yarns for Self-Charging Power Textiles. *Adv. Funct. Mater.* **2019**, *29*, 1806298.

(33) Pan, Z.; Yang, J.; Zhang, Q.; Liu, M.; Hu, Y.; Kou, Z.; Liu, N.; Yang, X.; Ding, X.; Chen, H.; Li, J.; Zhang, K.; Qiu, Y.; Li, Q.; Wang, J.; Zhang, Y. All-Solid-State Fiber Supercapacitors with Ultrahigh Volumetric Energy Density and Outstanding Flexibility. *Adv. Energy Mater.* **2019**, *9*, 1802753.

(34) Yang, B.; Chen, J.; Lei, S.; Guo, R.; Li, H.; Shi, S.; Yan, X. Spontaneous Growth of 3D Framework Carbon from Sodium Citrate for High Energy- and Power-Density and Long-Life Sodium-Ion Hybrid Capacitors. *Adv. Energy Mater.* **2018**, *8*, 1702409.

Recommended by ACS

Architecturally Robust Graphene-Encapsulated MXene Ti_2CT_x @Polyaniline Composite for High-Performance Pouch-Type Asymmetric Supercapacitor

Jianjian Fu, Kwang Ho Kim, *et al.*

SEPTEMBER 21, 2018
ACS APPLIED MATERIALS & INTERFACES

READ 

Heterostructural Three-Dimensional Reduced Graphene Oxide/CoMn₂O₄ Nanosheets toward a Wide-Potential Window for High-Performance Supercapac...

Cheng Zhang, Youwei Du, *et al.*

JULY 01, 2019
ACS APPLIED ENERGY MATERIALS

READ 

Understanding Integrated Graphene–MOF Nanostructures as Binder- and Additive-Free High-Performance Supercapacitors at Commercial Scale ...

Aditi Barua, Amit Paul, *et al.*

DECEMBER 12, 2021
ACS APPLIED ENERGY MATERIALS

READ 

Two-Dimensional Interface Engineering of Mesoporous Polydopamine on Graphene for Novel Organic Cathodes

Nan Wang, Yiyong Mai, *et al.*

JULY 02, 2019
ACS APPLIED ENERGY MATERIALS

READ 

Get More Suggestions >